*European Journal of Organic Chemistry*

WILEY VCH

EurJOC European Journal of Organic Chemistry | Chemistry Europe European Chemical Societies Publishing

RESEARCH ARTICLE OPEN ACCESS

# Experimental and Theoretical Investigations of Copper-Catalyzed Chemo-, Regio-, and Stereoselective *cis*-Hydroboration of 1,3-Enynes

Farshad Shiri[1] | Nicklas W. Buchbinder[2] | Andrew D. Bage[2] | Reilly Gwinn[2] | Carla Slebodnick[2] | Webster L. Santos[2] | Zhenyang Lin[1]

[1]Department of Chemistry, The Hong Kong University of Science and Technology, Kowloon, Hong Kong SAR, China | [2]Department of Chemistry, Virginia Tech, Blacksburg, Virginia, USA

**Correspondence:** Webster L. Santos (santosw@vt.edu) | Zhenyang Lin (chzlin@ust.hk)

**Received:** 14 October 2025 | **Revised:** 24 October 2025 | **Accepted:** 27 October 2025

**Funding:** Research Grants Council of Hong Kong, Grant/Award Numbers: HKUST 16300021 HKUST 16302222; National Science Foundation, Grant/Award Number: CHE-1726077

**Keywords:** 1,3-enynes | copper | DFT calculations | hydroboration | kinetics

## ABSTRACT

The mechanistic details of the chemo-, regio-, and stereoselective *cis*-hydroboration of 1,3-enynes were investigated using X-ray crystallography, kinetic analysis, and density functional theory (DFT) calculations. The kinetic analysis revealed that the reaction is first order in enyne, zeroth order in HBpin, and fractional order in the catalyst. Our studies suggest that a cyclic CuHBpinOAc complex is an off-cycle species (via DFT analysis) that contributes to the experimentally observed fractional rate order regarding the catalyst. Experimental and computational data suggest that hydrocupration is rate-limiting and essential for achieving selectivity.

## 1 | Introduction

Organoboron compounds have widespread usage in synthetic chemistry. Applications of these compounds in pharmaceutical science [1], total synthesis [2], agrochemical production [3], and material science [4] are being realized regularly. This trend highlights the ongoing need for synthetic methods to form boron–carbon bonds. The hydroboration of unsaturated bonds represents one of the most important strategies for incorporating boronic esters into carbon frameworks [5]. However, hydroboration reactions are often complicated by various reaction pathways that can result in poor chemo-, regio-, enantio-, or diastereoselectivity [6]. To address these complications, a great deal of research has been conducted on developing catalytic systems for achieving a high level of selectivity [7–11].

Transition-metal-catalyzed enyne hydroboration strategies can be broadly categorized into metal hydride or metal–boryl catalysis. Metal–boryl catalysis has been established to access 1,2- and 4,3-hydroboration products (Scheme 1) [12]. Theoretically, metal hydride catalysis could enable access to the orthogonal regioisomers, 2,1- and 3,4-hydroboration products. However, previously reported 1,3-enyne hydroboration methodologies involving metal hydride catalysts resulted in boryl-allenes (4,1 selectivity) or 1-boryl-1,3-dienes (4,3 selectivity) (Scheme 1) [8–10, 13]. Excluding our recent publication, a single report for accessing the 3,4-hydroboration product was established that relied on through-resonance polarization of the alkyne under copper-boryl conditions to afford 2-boryl-1,3-dieneoates [11]. Our group developed the chemo-, regio-, and stereoselective *cis*-hydroboration of nonpolar 1,3-enynes, unlocking access to

**Abbreviations:** CuCl, Copper chloride; CuOAc, Copper acetate; DFT, Density functional theory; HBpin, Pinacol borane; NMR, Nuclear magnetic resonance; VTNA, Variable time normalization analysis.

Farshad Shiri and Nicklas W. Buchbinder contributed equally to this work.

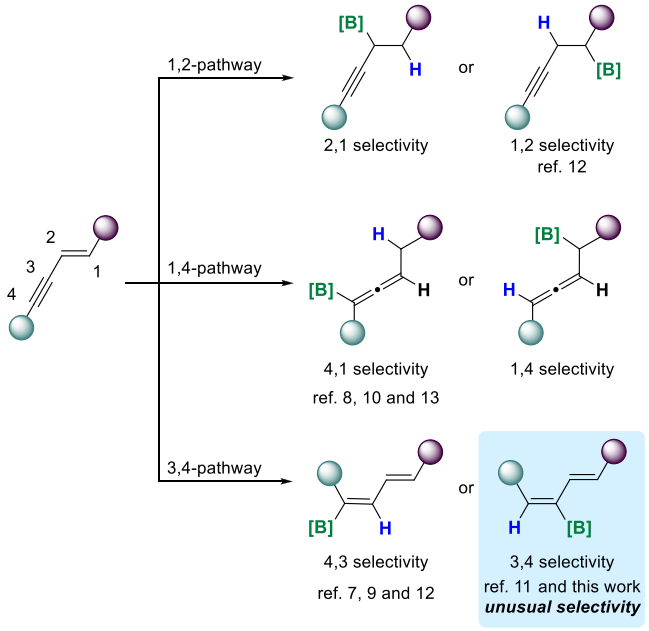


**SCHEME 1** | Possible regiochemical outcomes for 1,3-enyne hydroboration reactions. Chirality omitted for clarity.

the previously elusive (*Z*,*Z*)- and (*Z*,*E*)-2-boryl-1,3-dienes (3,4 selectivity) [14]. This reaction proceeds smoothly to afford 2-boryl-1,3-dienes as a single regioisomer with >99:1 *Z*:*E* selectivity. Because of our interest in the unique selectivity of this transformation, we sought to understand the underlying mechanistic intricacies and propose a catalytic cycle, using a combination of kinetic analysis, control reactions, X-ray crystallography, and computational modeling.

## 2 | Results and Discussion

Our investigation began by using Burés' variable time normalization analysis (VTNA) to determine the reaction orders of each reactant (Figure 1a) [15]. Formation of compound **P** was followed by $^1$H NMR spectroscopy for a series of "different excess" experiments, in which the initial concentration of three reagents was varied. Standard reaction conditions are as follows: 0.250 M **S**, 0.500 M HBpin, and 0.0125 M of CuOAc + Xantphos. Excess conditions evaluated for the kinetic study were 0.350 M **S**, 0.675 M HBpin, and 0.0250 M CuOAc + Xantphos. The reaction order of **S**, catalyst (CuOAc + Xantphos), and HBpin was determined by observing overlap between "[**P**] versus time" plots of standard and excess conditions when the time function was normalized with VTNA, and the correct order is used (see Supporting Information). The reaction was found to be first order in **S**, fractional order in CuOAc + Xantphos (0.7), and zeroth order in HBpin. When all "different excess" experiments were plotted together, a $K_{obs}$ graph was generated giving a $R^2$ of 0.91 (Figure 1a). The fractional rate order in CuOAc + Xantphos was corroborated by initial rate analysis (see Supporting Information). The zeroth order in HBpin and fractional order in CuOAc + Xantphos strongly suggests the presence of inactive off-cycle species likely in rapid equilibrium with the active catalyst [16, 17]. This equilibrium reduces the concentration of the active catalyst, resulting in a partial reaction order. Herein, we sought to determine the identity of the off-cycle species.

Copper hydride species are known to oligomerize or form dihydroboronate complexes with HBpin and could be the possible cause of the observed fractional rate order [18, 19]. Hartwig and coworkers found that a copper dihydroboronate species

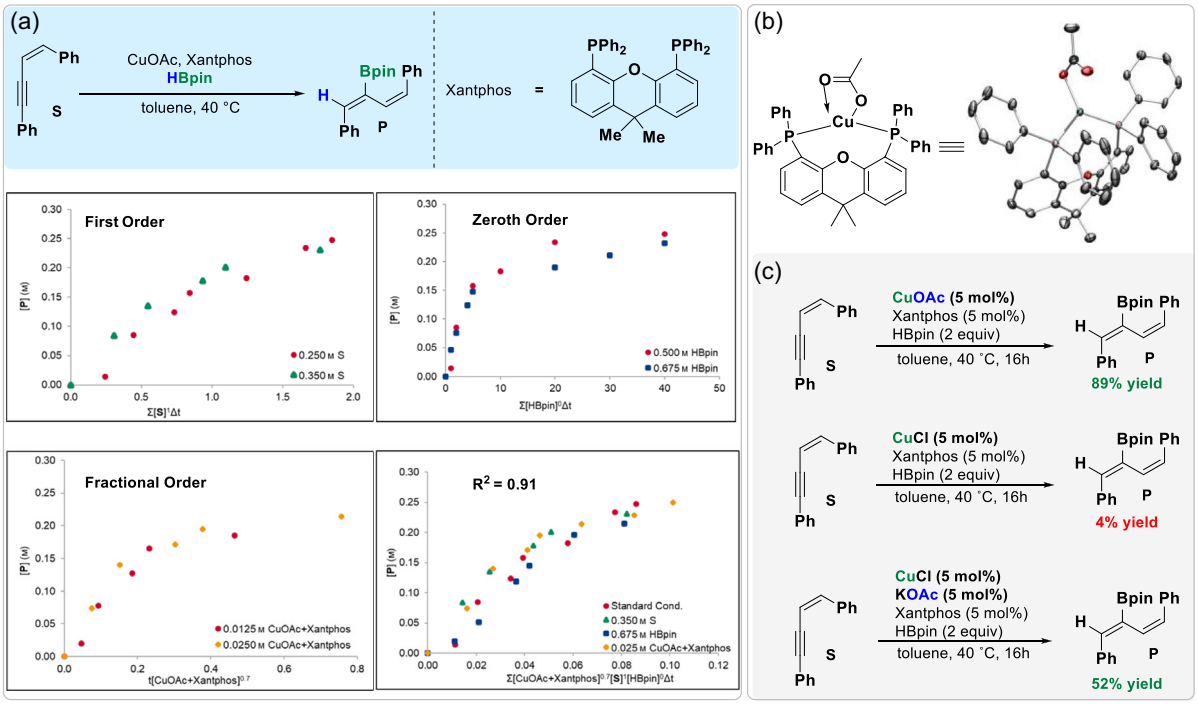


**FIGURE 1** | (a) Kinetic analysis of Cu(I)-catalyzed hydroboration of 1,3-enyne **S** using VTNA. (b) Crystal structure of complex **1** ([(Xantphos)Cu(OAc)]. (c) Standard reaction conditions, CuCl as catalyst, CuCl with acetate additive (KOAc).

was the resting-state catalyst in the copper hydride-catalyzed asymmetric hydroboration of internal alkenes [20]. However, we can rule out this type of complex because of the observed zeroth order in HBpin. Experiments using stoichiometric copper, ligand, and excess HBpin revealed an $^{11}$B NMR peak at 8.9 ppm, which is consistent with a tetrahedral boron species, possibly the off-cycle complex (see Supporting Information). Attempts to isolate the copper hydride catalyst species proved unsuccessful. However, we were successful in obtaining a crystal using one equivalent CuOAc, one equivalent of Xantphos, and two equivalents of HBpin in toluene. Singe-crystal X-ray diffraction analysis revealed a ligated copper acetate complex **1** (Figure 1b) [21]. Next, control experiments were performed to investigate and explain the vast difference in yields when various copper precatalysts were used. For example, CuOAc and CuCl afforded 89% and 4% yield, respectively (Figure 1c). When CuCl was used in the presence of KOAc (5 mol%), the yield improved to 52%, suggesting that the acetate counterion plays an essential role in the catalytic cycle, probably acting as a Lewis base for activating HBpin to transfer a hydride to the copper precatalyst to form the copper hydride complex. Indeed, the role of oxygen-donor Lewis bases for earth-abundant metal catalysis has been studied and is consistent with our experiments [22]. Taken together, our studies suggest that the off-cycle species may include a ligated copper acetate species that is complexed to HBpin.

To further explore this possibility in the reaction mechanism, we employed DFT calculations at the SMD(toluene)/M06D3/def2-TZVP//SMD/M06D3/SDD(toluene) ≈6–31G(d) level of theory. Our computational analysis was initiated by examining the mechanistic details for the transformation from the precatalyst **1** [(Xantphos)Cu(OAc)] to either the **Cu–H** or **Cu–Bpin** complex (Figure 2a). Two distinct pathways emerge: pathway *red* leads to **Cu–Bpin** while pathway *black* leads to the **Cu–H** complex. Pathway *red* is initiated by the coordination of HBpin to **1**, resulting in the formation of **4**. The elongation of the B—H bond in the adduct (1.196 Å) from this bond in HBpin (1.187 Å) signifies the donation of the B—H $\sigma$-bonding electron pair to the unoccupied p orbital on the copper center in **4**. Complex **4** then transforms into **Cu–Bpin** with a very high barrier of 26.0 kcal/mol via the deprotonation transition structure $\mathbf{TS_{4\text{-}CuBOAc}}$. The very high barrier here is expected since H-Bpin shows hydridic but not protic reactivity. In contrast, pathway *black* also involves HBpin's boron coordinating to the pendant oxygen on the coordinated acetate in **1**, resulting in the formation of **2.** The B—H bond length in this adduct (1.193 Å) is slightly longer than that in HBpin, a result related to both the participation of the B—H $\sigma$-bonding electron pair in the donation to the vacant p orbital on the copper center and the notable B—O interaction (an O—B bond distance of 2.579 Å).

In the presence of HBpin, complex **2** converts to intermediate **3** through transition structure $\mathbf{TS_{2\text{–}3}}$, overcoming a barrier as low as 3.4 kcal/mol. Intermediate **3** is the lowest energy complex calculated (−7.5 kcal/mol), which has all of the components of an off-cycle species suggested by our experimental studies (*vide supra*). The same structure was proposed in a recent computational study performed by the Zhang group [23]. The acetate ligand plays a crucial role in stabilizing this off-cycle species, which bridges the HBpin boron and the copper center. Indeed, the absence of acetate in our experimental work results in decreased yield. The **Cu–H** complex can be generated from **3** by releasing

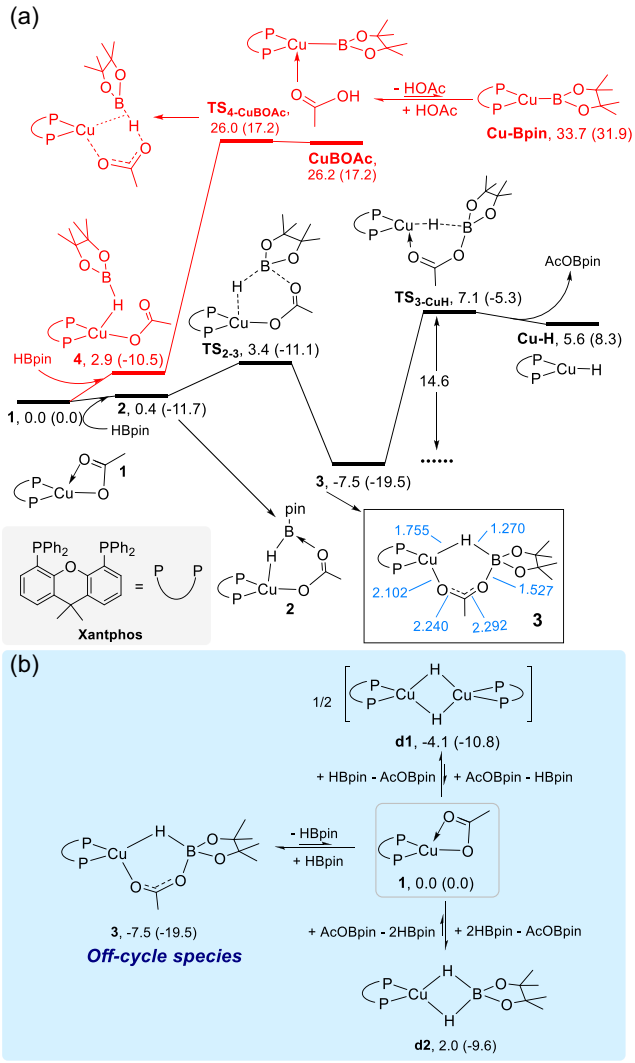


**FIGURE 2** | (a) Calculated free energy profile for transformation of the precatalyst 1 to the Cu–H or Cu–Bpin complex. The blue values represent the length of selective bonds in Å. (b) Calculated relative free energies for dimeric species in equilibrium with the copper hydride complex Cu–H. Relative Gibbs free energies and relative electronic energies (in parenthesis) are given in kcal/mol.

**AcOBpin** through the transition structure $\mathbf{TS_{3\text{-}CuH}}$. Figure 2a clearly shows that the generation of the **Cu–H** complex is much more favorable both kinetically and thermodynamically than that of **Cu–Bpin** and that **Cu–Bpin** is energetically inaccessible.

We have also examined the scenarios where the formed copper hydride complex **Cu–H** can potentially exist in equilibrium with the dimeric species **d1** and **d2** (Figure 2b). Our calculations reveal that both the dimeric species **d1** and **d2** are energetically less stable when compared to **3**.

Figure 3 shows the energy profiles calculated for the reaction starting from **Cu–H**. Upon formation of **Cu–H**, the enyne substrate **S** coordinates to the copper center, either through its alkyne or alkene moiety.

The alkyne coordination can proceed through two distinct pathways: one leading to structure **5** (Figure 3a, pathway *black*) and

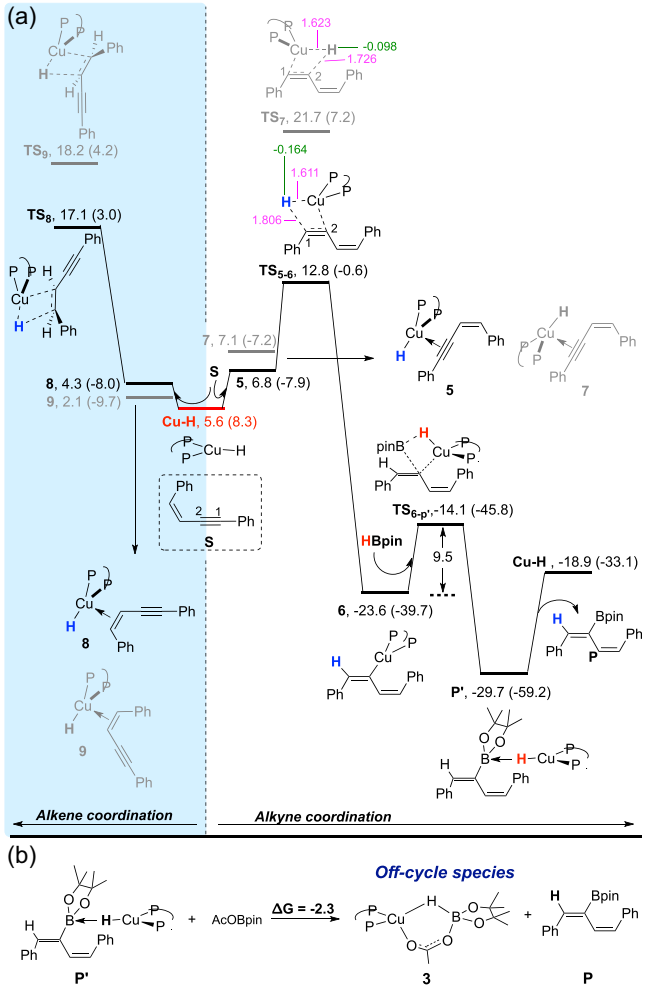


**FIGURE 3** | (a) Calculated free energy profile for the borylation of substrate **S**. The pink values represent the length of selective bonds in Å. The green values represent the NBO charge of selected atoms. Relative Gibbs free energies and relative electronic energies (in parenthesis) are given in kcal/mol. (b) Comparison of the energies of **P′** and **3**. Relative Gibbs free energy is given in kcal/mol.

the other leading to structure **7** (Figure 3a, pathway *gray*). The formation of the alkyne-coordinated species **5** is endergonic by 1.2 kcal/mol compared to **Cu—H** (Figure 3a, pathway *black*). From **5**, hydrocupration, i.e., alkyne insertion into the **Cu—H** bond, occurs on the **Cu**-coordinated alkyne moiety via the transition structure $\mathbf{TS_{5–6}}$, resulting in the formation of the intermediate **6**.

In the alternative pathway involving alkene coordination followed by insertion into the **Cu—H** bond, alkene insertion exhibits a substantially higher activation barrier compared to alkyne insertion (Figure 3a). The preference for alkyne hydrocupration can be attributed to preservation of the conjugated $\pi$-system during alkyne coordination, whereas alkene hydrocupration would disrupt the extended conjugation and be sterically less favorable, resulting in an unfavorable pathway.

Intermediate **6** subsequently undergoes metathesis through transition structure $\mathbf{TS_{6\text{-}P'}}$ with an energy barrier of 9.5 kcal/mol. This leads to the formation of complex **P′**, which subsequently dissociates to afford the final product **P** and regenerate the **Cu–H** complex.

Figure 3a clearly shows that the transition structures $\mathbf{TS_{5–6}}$ lie lower in energy than the transition structures $\mathbf{TS_7}$, demonstrating the more favorable nature of pathway *black*. NBO analysis reveals that the hydride ligand in $\mathbf{TS_{5–6}}$ carries a more negative charge than its counterpart in $\mathbf{TS_7}$ (Figure 3a), indicating a greater nucleophilicity of the hydride in $\mathbf{TS_{5–6}}$. Additionally, the extended $\pi$-conjugation present in $\mathbf{TS_{5–6}}$ provides a more effective pathway for charge delocalization during hydride migration to C1, whereas the corresponding charge transfer to C2 in $\mathbf{TS_7}$ occurs through a less conjugated system. Therefore, the hydrocupration step serves as the regioselectivity-determining step of the reaction.

Utilizing the energetic span model and its refinement [24, 25], Figure 3a indicates that $\mathbf{TS_{5–6}}$ is the rate-determining transition state and the overall energy barrier for the catalytic reaction is determined to be 18.0 kcal/mol {=(12.8 − 5.6) + [(18.9) − (−29.7)]}.

The rate-determining transition state $\mathbf{TS_{5–6}}$ involves the insertion of the alkyne substrate into the active catalyst's **Cu—H** bond, and is not influenced by the reactant HBpin. This finding aligns perfectly with the reaction's rate order, which is first order in **S** and zeroth order in HBpin (Figure 1). Considering the nature of the rate-determining transition state, one would anticipate that the rate order with respect to the catalyst is also first order. However, the observed fractional rate order of 0.7 concerning the catalyst (Figure 1) suggests that the reaction rate is not directly proportional to the catalyst concentration. As shown in Figure 2a, we found that intermediate **3** exhibits notable stability in relation to the active species **Cu–H**. Moreover, as shown in Figure 3b, **P′**, a product-coordinated species within the catalytic cycle, can combine with AcOBpin that was produced in catalytic amounts during the generation of the **Cu–H** active species (Figure 2a), to give **3**, an off-cycle species as previously mentioned. The experimentally observed fractional rate order regarding the CuOAc + Xantphos (0.7) can be rationalized by the existence of the proposed off-cycle complex.

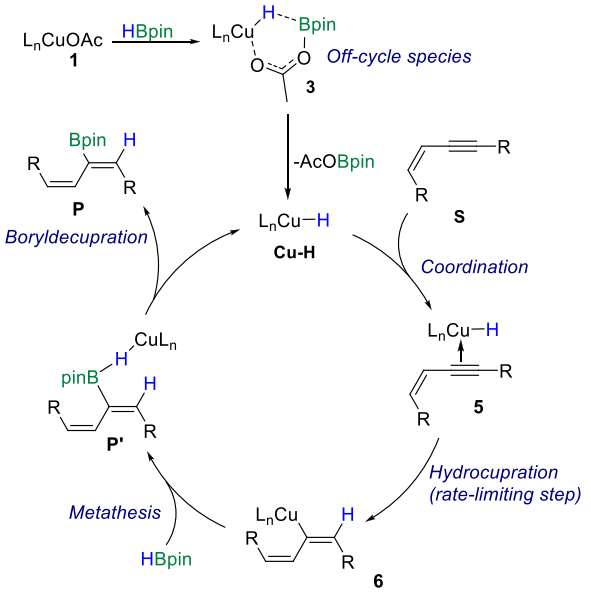


**SCHEME 2** | Proposed mechanism of 1,3-enyne hydroboration based on experimental and computational studies.

Based on experimental and computational studies, a catalytic cycle for the (*Z*)-3,4-hydroboration of 1,3-enynes is proposed (Scheme 2). In the presence of a ligand and a Lewis base (acetate), the copper precatalyst **1** reacts with HBpin, forming the active species **Cu–H**. **Cu–H** is derived from intermediate **3**, which is an off-cycle species. Coordination of enyne **S** with **Cu–H** results in complex **5.** Hydrocupration of complex **5** forms vinyl cuprate **6** as the rate-limiting step of the catalytic cycle. Then, **6** undergoes a metathesis reaction to generate complex **P′**, which subsequently dissociates to afford final product **P** and regenerate the **Cu–H** active species**.**

## 3 | Conclusion

In conclusion, the mechanistic complexities of the chemo-, regio-, and stereoselective *cis*-hydroboration of 1,3-enynes were investigated. Kinetic analysis and computational studies suggest that hydrocupration is rate limiting and essential for achieving a high level of selectivity. Experimental studies revealed the importance of acetate for reactivity. Further, kinetic studies suggest a fractional rate order in the catalyst and a zeroth order in HBpin. These observations can be rationalized by a more stable off-cycle CuHBpinOAc complex, which is supported by our computational investigation.

## 4 | Experimental Section/Methods

Each experiment was run in duplicate and averaged. To a flame-dried and sealed 2-dram vial: a stir bar, 250 µl of a 0.025 M solution of CuOAc (0.05 equiv., 6.25 µmol) and Xantphos (0.05 equiv., 6.25 µmol) in dichloromethane (DCM) were added. The DCM was removed under vacuum and the vial was put under inert atmosphere using standard *Schlenk* technique. Then, 500 µl of a 0.250 M solution of enyne **S** (1.0 equiv., 0.125) and 0.125 M solution of 1,2,4,5-tetramethylbenzene (internal standard, 0.50 equiv., 0.0625 mmol) in toluene was added. Finally, pinacolborane (2.0 equiv., 0.250 mmol) was added and a timer was started. Aliquots (10 µl) of the reaction were removed at recorded times, exposed to air, and diluted in $CDCl_3$. Formation of 2-boryl-1,3-diene **P** was tracked via $^1H$ NMR with 1,2,4,5-tetramethylbenzene as an internal standard.

[CCDC 2377607 contains the supplementary crystallographic data for this paper. These data can be obtained free of charge from The Cambridge Crystallographic Data Centre via www.ccdc.cam.ac.uk/data_request/cif.].

[Further details of the crystal structure investigation may be obtained from the Fachinformationszentrum Karlsruhe, 76344 Eggenstein-Leopoldshafen (Germany), on quoting the depository number CSD 2377607].


### Acknowledgments

The authors thank the support of the National Science Foundation (CHE-1726077), Virginia Tech Research and Innovation (ADB), and the Research Grants Council of Hong Kong (HKUST 16302222).


### Conflicts of Interest

The authors declare no conflicts of interest.

### Data Availability Statement

The data that support the findings of this study are available from the corresponding author upon reasonable request.

### References


1. R. J. Grams, W. L. Santos, I. R. Scorei, et al., *Chemical Reviews* 124 (2024): 2441–2511.

2. Y. Watanabe, H. Morozumi, H. Mutoh, K. Hagiwara, and M. Inoue, *Angewandte Chemie International Edition* 135 (2023): e202309688.

3. L. Li, G. Bai, W. Gu, et al., *Industrial Crops and Products* 221 (2024): 119336.

4. H. Wang, Z. Shi, K. Guo, et al., *Macromolecules* 56 (2023): 2494–2504.

5. S. K. Bose, L. Mao, L. Kuehn, et al., *Chemical Reviews* 121 (2021): 13238–13341.

6. L. Mao and S. K. Bose, *Advanced Synthesis & Catalysis* 362 (2020): 4174–4188.

7. S. Xu, Y. Zhang, B. Li, and S.-Y. Liu, *Journal of the American Chemical Society* 138 (2016): 14566–14569.

8. Y. Huang, J. Del Pozo, S. Torker, and A. H. Hoveyda, *Journal of the American Chemical Society* 140 (2018): 2643–2655.

9. Y. Jia, L. Yang, X. Wang, W. Yang, and W. Zhao, *Organic Letters* 26 (2024): 3258–3262.

10. H. L. Sang, S. Yu, and S. Ge, *Organic Chemistry Frontiers* 5 (2018): 1284–1287.

11. F.-F. Meng, Q.-Y. Xue, B. Jiang, et al., *Organic Letters* 21 (2019): 2932–2936.

12. Y. Sasaki, Y. Horita, C. Zhong, M. Sawamura, and H. Ito, *Angewandte Chemie International Edition* 50 (2011): 2778–2782.

13. D.-W. Gao, Y. Xiao, M. Liu, et al., *ACS Catalysis* 8 (2018): 3650–3654.

14. N. W. Buchbinder, L. H. Nguyen, O. N. Beck, A. D. Bage, C. Slebodnick, and W. L. Santos, *Organic Letters* 26 (2024): 6136–6141.

15. J. Burés, *Angewandte Chemie International Edition* 128 (2016): 16318–16321.

16. R. J. Somerville, L. V. Hale, E. Gómez-Bengoa, J. Burés, and R. Martin, *Journal of the American Chemical Society* 140 (2018): 8771–8780.

17. T. Rosner, J. Le Bars, A. Pfaltz, and D. G. Blackmond, *Journal of the American Chemical Society* 123 (2001): 1848–1855.

18. D. A. Kutateladze, B. K. Mai, Y. Dong, Y. Zhang, P. Liu, and S. L. Buchwald, *Journal of the American Chemical Society* 145 (2023): 17557–17563.

19. C.-Y. Liu, S.-F. Yuan, S. Wang, Z.-J. Guan, D.-e. Jiang, and Q.-M. Wang, *Nature Communications* 13 (2022): 2082.

20. Y. Xi and J. F. Hartwig, *Journal of the American Chemical Society* 139 (2017): 12758–12772.

21. Deposition number 2377607 contains the supplementary crystallographic data for this paper. These data are provided free of charge by the joint Cambridge Crystallographic Data Centre Fachinformationszentrum Karlsruhe Access Structures service www.ccdc.cam.ac.uk/structures.

22. J. H. Docherty, J. Peng, A. P. Dominey, and S. P. Thomas, *Nature Chemistry* 9 (2017): 595–600.

23. L. Zhang, S. Li, Y. Wen, et al., *Asian Journal of Organic Chemistry* 14 (2025): e202400430.

24. Y. Li and Z. Lin, *Organic Chemistry Frontiers* 1 (2014): 1188–1196.

25. S. Kozuch and S. Shaik, *Accounts of Chemical Research* 44 (2011): 101–110.

## Supporting Information

Additional supporting information can be found online in the Supporting Information section. **Supporting Fig. S1:** Reaction progress profile of standard conditions. Initial concentrations: [**S**] = 0.250 M, [HBpin] = 0.500 M, [CuOAc + Xantphos] = 0.0125 M. **Supporting Fig. S2a:** Time normalized reaction progress profile of excess **S** (0.350 M). Initial concentrations for excess conditions: [**S**] = 0.350 M, [HBpin] = 0.500 M, [CuOAc + Xantphos] = 0.0125 M. **Supporting Fig. S2b:** Time normalized reaction progress profile of excess **S** (0.350 M). Initial concentrations for excess conditions: [**S**] = 0.350 M, [HBpin] = 0.500 M, [CuOAc + Xantphos] = 0.0125 M. **Supporting Fig. S2c:** Time normalized reaction progress profile of excess **S** (0.350 M). Initial concentrations for excess conditions: [**S**] = 0.350 M, [HBpin] = 0.500 M, [CuOAc + Xantphos] = 0.0125 M. **Supporting Fig. S3a:** Time normalized reaction progress profile of excess CuOAc + Xantphos (0.025 M). Initial concentrations for excess conditions: [**S**] = 0.250 M, [HBpin] = 0.500 M, [CuOAc + Xantphos] = 0.0250 M. **Supporting Fig. S3b:** Time normalized reaction progress profile of excess CuOAc + Xantphos (0.025 M). Initial concentrations for excess conditions: [**S**] = 0.250 M, [HBpin] = 0.500 M, [CuOAc + Xantphos] = 0.0250 M. **Supporting Fig. S3c:** Time normalized reaction progress profile of excess CuOAc + Xantphos (0.025 M). Initial concentrations for excess conditions: [**S**] = 0.250 M, [HBpin] = 0.500 M, [CuOAc + Xantphos] = 0.0250 M. **Supporting Fig. S3d:** Time normalized reaction progress profile of excess CuOAc + Xantphos (0.025 M). Initial concentrations for excess conditions: [**S**] = 0.250 M, [HBpin] = 0.500 M, [CuOAc + Xantphos] = 0.0250 M. **Supporting Fig. S4:** Initial Rate vs. $[CuOAc + Xantphos]_0$. Initial Concentrations: [**S**] = 0.250 M, [HBpin] = 0.500 M, [CuOAc + Xantphos] = 0.000, 0.006, 0.0125, 0.0188, 0.0250, 0.0625 M. **Supporting Fig. S6a:** Time normalized reaction progress profile of excess HBpin (0.675 M). Initial concentrations for excess conditions: [**S**] = 0.250 M, [HBpin] = 0.675 M, [CuOAc + Xantphos] = 0.0250 M. **Supporting Fig. S6b:** Time normalized reaction progress profile of excess HBpin (0.675 M). Initial concentrations for excess conditions: [**S**] = 0.250 M, [HBpin] = 0.675 M, [CuOAc + Xantphos] = 0.0250 M. **Supporting Fig. S6c:** Time normalized reaction progress profile of excess HBpin (0.675 M). Initial concentrations for excess conditions: [**S**] = 0.250 M, [HBpin] = 0.675 M, [CuOAc + Xantphos] = 0.0250 M. **Supporting Fig. S7a:** $K_{obs}$ Plot. Initial concentrations: Red: [**S**] = 0.250 M, [HBpin] = 0.500 M, [CuOAc + Xantphos] = 0.0125 M. Green [**S**] = 0.350 M, [HBpin] = 0.500 M, [CuOAc + Xantphos] = 0.0125 M. Blue [**S**] = 0.250 M, [HBpin] = 0.675 M, [CuOAc + Xantphos] = 0.0125 M. Yellow [**S**] = 0.250 M, [HBpin] = 0.500 M, [CuOAc + Xantphos] = 0.0250 M. **Supporting Fig. S7b:** $K_{obs}$ Plot. Initial concentrations: Red: [**S**] = 0.250 M, [HBpin] = 0.500 M, [CuOAc + Xantphos] = 0.0125 M. Green [**S**] = 0.350 M, [HBpin] = 0.500 M, [CuOAc + Xantphos] = 0.0125 M. Blue [**S**] = 0.250 M, [HBpin] = 0.675 M, [CuOAc + Xantphos] = 0.0125 M. Yellow [**S**] = 0.250 M, [HBpin] = 0.500 M, [CuOAc + Xantphos] = 0.0250 M. **Supporting Fig. S8:** $^{11}B$ NMR for stoichiometric CuOAc and Xantphos reaction with excess pinacolborane. Pinacolborane appears as a doublet because this is a $^{1}H$ coupled $^{11}B$ NMR experiment. **Supporting Fig. S9:** $^{11}B$ NMR for stoichiometric CuOAc reaction with excess pinacolborane. Pinacolborane appears as a doublet because this is a $^{1}H$ coupled $^{11}B$ NMR experiment. **Supporting Fig. S10:** Solid-state molecular structures for [Cu(Xantphos)(OAc)] (**1**), (with anisotropic displacement ellipsoids at 50% probability level. Color scheme: Cu, green; P, pink; O, red C, gray. Hydrogens and solvent molecules are omitted for clarity. **Supporting Table S1:** Concentration Data for Standard Conditions Reaction Progress Profile. **Supporting Table S2:** Concentration Data for Excess (0.350 M) **S** Conditions. **Supporting Table S3:** Concentration Data for Excess (0.0250 M) CuOAc + Xantphos Conditions. **Supporting Table S4:** Initial Rate Data for CuOAc + Xantphos. Rate Order Determination. **Supporting Table S6:** Concentration Values Determined by $^{1}H$ NMR for Initial Rates. **Supporting Table S7:** Concentration Data for Excess (0.675 M) HBpin Conditions. **Supporting Table S8:** Concentration Data for $K_{obs}$ Graph. **Supporting Table S9:** X-ray diffraction experimental details.